



Mapping urban forest leaf area index with airborne lidar using penetration metrics and allometry

Michael Alonzo ^{a,*}, Bodo Bookhagen ^b, Joseph P. McFadden ^a, Alex Sun ^a, Dar A. Roberts ^a

^a Department of Geography, University of California Santa Barbara, Santa Barbara, CA 93106, USA

^b University of Potsdam, Institute of Earth and Environmental Science, Karl-Liebknecht-Str. 24-25, 14467 Potsdam-Golm, Germany



ARTICLE INFO

Article history:

Received 25 August 2014

Received in revised form 26 January 2015

Accepted 16 February 2015

Available online xxxx

Keywords:

Airborne lidar

Leaf area index

Urban ecosystem analysis

Hemispherical photography

Allometry

Vegetation structure

ABSTRACT

In urban areas, leaf area index (LAI) is a key ecosystem structural attribute with implications for energy and water balance, gas exchange, and anthropogenic energy use. In this study, we estimated LAI spatially using airborne lidar in downtown Santa Barbara, California, USA. We implemented two different modeling approaches. First, we directly estimated effective LAI (LAI_e) using scan angle- and clump-corrected lidar laser penetration metrics (LPM). Second, we adapted existing allometric equations to estimate crown structural metrics including tree height and crown base height using lidar. The latter approach allowed for LAI estimates at the individual tree-crown scale. The LPM method, at both high and decimated point densities, resulted in good linear agreement with estimates from ground-based hemispherical photography ($r^2 = 0.82$, $y = 0.99x$) using a model that assumed a spherical leaf angle distribution. Within individual tree crown segments, the lidar estimates of crown structure closely paralleled field measurements (e.g., $r^2 = 0.87$ for crown length). LAI estimates based on the lidar crown measurements corresponded well with estimates from field measurements ($r^2 = 0.84$, $y = 0.97x + 0.10$). Consistency of the LPM and allometric lidar methods was also strong at 71 validation plots ($r^2 = 0.88$) and at 450 additional sample locations across the entire study area ($r^2 = 0.72$). This level of correspondence exceeded that of the canopy hemispherical photography and allometric, ground-based estimates ($r^2 = 0.53$). The first-order alignment of these two disparate methods may indicate that the error bounds for mapping LAI in cities are small enough to pursue large scale, spatially explicit estimation.

© 2015 Elsevier Inc. All rights reserved.

1. Introduction

Urban trees provide a broad array of ecosystem services that are governed by tree species, canopy structure, and locational context (Escobedo & Nowak, 2009; Manning, 2008; McCarthy & Pataki, 2010; McPherson, Simpson, Xiao, & Wu, 2011; Simpson, 2002; Urban, 1992). Leaf Area Index (LAI), commonly defined as one half of the total green leaf area per unit ground area (Chen & Black, 1992), is a critical structural attribute that has implications for urban energy balance, gas exchange, hydrological throughput, and anthropogenic energy use. It is an eco-physiological measure of leaf surface available for photosynthesis and transpiration (Chen, Rich, Gower, Norman, & Plummer, 1997). In addition, dry depositional uptake and intercellular suspension of air pollutants such as O_3 , NO_2 , SO_2 , CO , and PM_{10} is partly mediated by effective leaf surface area (Baldocchi, Hicks, & Camara, 1987; Hirabayashi, Kroll, & Nowak, 2011). In urban areas, this process has been related to spatial variation in air pollution reduction (e.g., Escobedo & Nowak, 2009). Increased canopy leaf area, especially over paved surfaces, delays stormwater peak flow through interception of precipitation (Xiao &

McPherson, 2002). Higher urban vegetation fractional cover (Lu & Weng, 2006; Myint, Brazel, Okin, & Buyantuyev, 2010) and higher LAI (Georgi & Zafiriadis, 2006; Hardin & Jensen, 2007; Oke, 1989; Peters & McFadden, 2010) have been correlated with lowered urban temperatures and reduced summertime building cooling costs. At the same time, tree cover has also been linked to ecosystem disservices ranging from pollen allergies to sidewalk damage and the production of litterfall (Roy, Byrne, & Pickering, 2012).

Many cities have estimated urban LAI using the USDA Forest Service's Urban Forest Effects (UFORE) model (Nowak, Crane, et al., 2008). The UFORE model produces estimates of urban forest structure, including LAI, and ecosystem function using field measurements of tree species and crown dimensions acquired on ≥200 stratified random inventory plots across a city (Nowak, Crane, et al., 2008). The resulting estimates of ecosystem function are used by cities for urban forest management and planning (e.g., Million Trees LA: McPherson et al., 2011). However, the data collection process is labor intensive, and the results are only available at very coarse spatial resolution. Further, the LAI estimates become increasingly uncertain in regions where the model's allometric equations have not been parameterized by locally-evaluated, species-specific coefficients (Gower, Kucharik, & Norman, 1999; Peper & McPherson, 2003). By contrast, the estimation of effective

* Corresponding author. Tel.: +1 805 883 8821.

E-mail address: mike.alonzo@geog.ucsb.edu (M. Alonzo).

LAI (LAI_e) in an urban area from hemispherical photography (hereafter “hemiphotos”) may be more robust to the varying mixtures of tree species than allometric methods. LAI_e differs from true LAI in that it does not account for the non-random distribution of foliage throughout the canopy and does not differentiate between foliar and woody plant components (Chen & Black, 1991). However, measurement challenges such as discontinuous canopy cover, variability in canopy height, occlusion of foliage by buildings and other structures, and difficulty of accessing private property at times when sky conditions are appropriate for the method have limited the use of this technique in cities (Jensen, Hardin, & Hardin, 2012; Jensen et al., 2009; Osmond, 2009; Peper & McPherson, 2003; Richardson, Moskal, & Kim, 2009). Importantly, both allometry and hemispherical photography are field-sampling techniques that generate only point estimates of LAI that cannot easily be extended to a citywide map. Remote sensing data can be used to estimate and map urban LAI and LAI_e over large areas at fine spatial scales, possibly at significant cost savings compared to field campaigns (Nowak, Walton, Stevens, Crane, & Hoehn, 2008).

Maps of LAI_e in natural forest settings are frequently produced using laser penetration metrics (LPM) calculated from airborne lidar (e.g., Hopkinson et al., 2013; Korhonen, Korpela, Heiskanen, & Maltamo, 2011; Solberg et al., 2009; Zhao & Popescu, 2009). LPMs, which report the penetration ratios of laser pulses through canopy, are favored in part due to the theoretical reliance on Beer-Lambert's law of light attenuation that they share with gap fraction calculated from hemiphotos. However, issues related to multi-scale clumping of foliage, the variable relationship between sensor scan angle and canopy path length, and the wide range of possible leaf angle distributions due to species diversity have largely precluded lidar mapping of LAI_e in heterogeneous areas (Holmgren, Nilsson, & Olsson, 2003; Morsdorf, Frey, Meier, & Itten, 2008; Van Gardingen, Jackson, Hernandez-Dumas, Russell, & Sharp, 1999). Despite these limitations, Richardson et al. (2009) showed that mapping LAI_e was possible in a biodiverse urban park and that the assumption of a spherical leaf angle distribution may be acceptable.

In this study we sought to improve LAI mapping capabilities in heterogeneous urban environments. We used two theoretically distinct modeling approaches and multiple types of validation evidence. It is important to acknowledge that indirect, ground-based measurements of LAI or LAI_e are problematic, exhibiting variability and bias with respect to true LAI and each other (Bréda, 2003; Peper & McPherson, 2003). We first examined the relationship between lidar estimates of LAI_e using a Beer-Lambert style approach and estimates from hemiphotos acquired at 71 field plots. Second, we adapted the allometric equations used in the UFORE model for use with crown dimension measurements (e.g., height, diameter) taken at the individual tree crown scale (hereafter “crown scale”) using lidar. The specific objectives of this study were:

1. Map LAI_e in a heterogeneous, urban landscape at the field-plot scale through correlation of LPM derived LAI_e and hemiphoto gap fraction inversion.
2. Introduce methods for mitigating the effects of off-nadir lidar pulse angles and non-random foliage distribution on estimates of LAI_e in discontinuous canopy.
3. Map LAI of individual trees using automatically delineated crown objects, lidar-measured crown dimensions, and an allometric approach.
4. Compare plot-aggregated allometric LAI outputs with the plot-level outputs from the LPM method to characterize the covariation.

We anticipated that the plot-level metrics based on Beer-Lambert's law would offer a site-transferable means to estimate LAI_e with minimal model calibration from field data. This output could be useful for broad assessment and modeling of urban surface energy balance in terms of heat, moisture, and momentum fluxes (Grimmond et al., 2010) However, the resultant map resolution will not allow for estimates of urban tree ecosystem service provision in the manner desired by many cities (i.e., services that depend on crown location relative to buildings and impervious surfaces). Crown scale estimates of LAI validated against

UFORE allometry offer a more direct path towards a spatially explicit urban forest inventory albeit one that internalizes the uncertainties of the UFORE model.

2. Materials and methods

2.1. Study area and field plots

This study was conducted in downtown Santa Barbara, California (34.42°N , 119.69°W) (Fig. 1). Santa Barbara is a city of about 90,000 residents, encompassing 51 km^2 , located on a coastal plain between the Pacific Ocean to the south and the Santa Ynez mountains to the north. It has a Mediterranean climate and supports a diverse mix of native, introduced, and invasive urban forest species. Fractional canopy cover ($f\text{Cov}$) was estimated in 2012 at 25.4% for the entire municipality of Santa Barbara using high-resolution digital imagery (City of Santa Barbara Urban Forest Management Plan, 2014, www.santabarbaraca.gov). Our study area was situated in the most densely built portion of the city and, according to UFORE estimates in 2012, $f\text{Cov}$ was approximately 20%.

In the fall of 2012, we inventoried vegetation within 105 plots, recording 108 unique species. The most commonly sampled species were the broadleaf persistent native *Quercus agrifolia* (Coast live oak) and the introduced *Syagrus romanzoffiana* (Queen palm). Each plot (Fig. 1) had a radius of 11.4 m in accordance with UFORE data collection protocols (i-Tree Eco User's Manual v. 4.1.0, www.itreetools.org). Species composition and structure in the plots was extremely heterogeneous: Thirty-eight plots had LAI values of <1 and 10 plots had values >3 (mean = 1.39). Average canopy height was also highly variable, ranging between 2 and 23 meters with significant internal variation as well. The number of trees per plot ranged between 1 and 57 with a median stem count of 4 trees. Plot centers were geolocated using differentially corrected GPS and were positionally accurate to 30 cm with respect to the lidar data. The distance and direction of each stem was measured from plot center with an Opti-Logic laser range finder and a compass. Of the 105 sampled plots, 71, with colocated field measurements, hemiphotos, and lidar data were retained for analysis.

2.2. LAI_e estimates from hemispherical photography

To characterize the extreme heterogeneity in urban forest gap fraction, one hemiphotograph was acquired at plot center along with four additional photos 5.5 m from the center in each cardinal direction. Plots where only one photo site was accessible represented 16% of the total. While best practice dictates that hemiphotos are acquired under diffuse light conditions, this was not always possible. Southern California autumn days are frequently cloudless and the high likelihood of a field plot falling on private property limited our flexibility in acquisition time. The photos were taken at 1 m above ground using a Nikon Coolpix 5400 digital camera retrofitted by removing the manufacturer's infrared-blocking filter and replacing it with a filter that blocked wavelengths $<590 \text{ nm}$ such that it could record red and infrared light. The modified camera was used because hemiphotos acquired with near infrared (NIR) wavelengths can lead to more efficient and accurate image binarization of foliage (Chapman, 2007). This advantage is important in urban settings where hemiphotos frequently contain structures interspersed with foliage (Osmond, 2009).

At each hemiphotograph location, we acquired images at three exposure settings: 1-stop underexposed, automatic exposure, and 1-stop overexposed. We combined these multiple exposures into a single high-dynamic range (HDR) image to enhance contrast between foliage and sky (Jonckheere, Nackaerts, Muys, & Coppin, 2005; Zhang, Chen, & Miller, 2005) and mitigate pixel saturation caused by direct beam radiation (Korhonen et al., 2011). HDR processing was completed with minimal changes to default settings in Dynamic-Photo HDR 5 (v 5.2.0). Foliage, plant stems, and branches were distinguished from all other

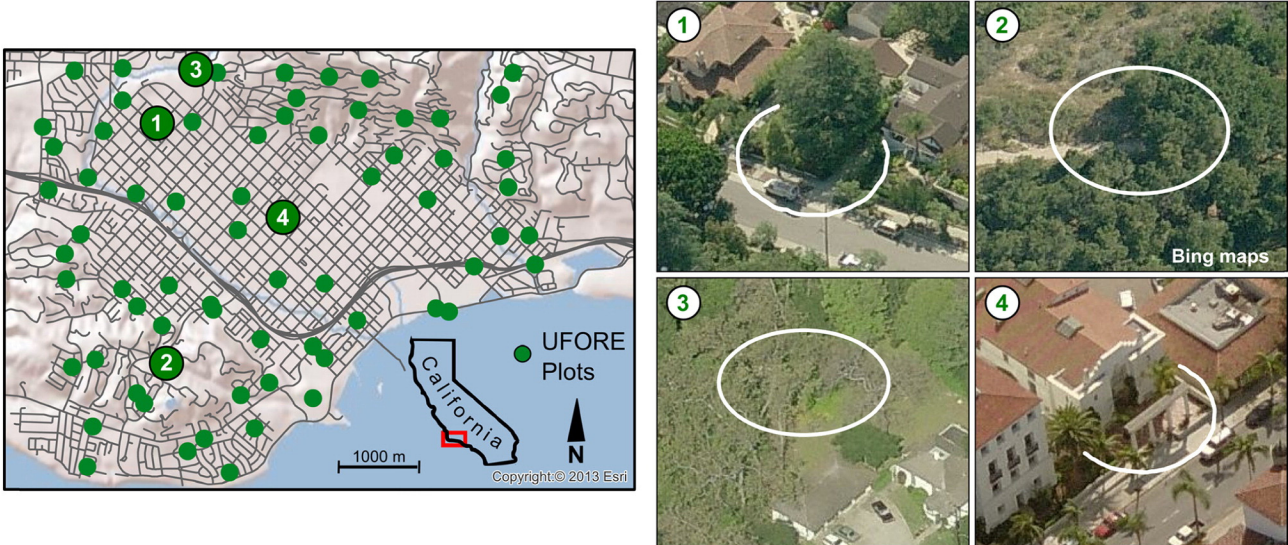


Fig. 1. Study area located in downtown Santa Barbara, California. Green dots show grid-randomized distribution of 71 field plots. The shaded topographic relief background shows that most plots are on flat ground but some, in the northeast and southwest are on steep slopes. At right, oblique angle aerial imagery courtesy of Bing Maps showing 4 representative 11.4 m radius plots.

scene components through an image segmentation rule-set applied to the hemiphotos using Trimble's eCognition software (v. 6.4, Munich, Germany). Multi-resolution segmentation and locally-thresholded classification allowed us to address variability in scene illumination and the complex mix of biotic and abiotic scene elements (Jonckheere et al., 2004). Nevertheless, as these photos were used for validation of remotely sensed estimates, some manual editing was required.

Gap fraction was calculated from the binary images at zenith bin midpoints ($7^\circ, 23^\circ, 38^\circ, 53^\circ$, and 68°) that, for compatibility with previous research (e.g., Korhonen et al., 2011; Solberg et al., 2009), correspond with the concentric detector rings of the LAI-2000 Plant Canopy Analyzer (Li-Cor, Lincoln, Nebraska, USA). LAI_e can be calculated from gap fraction using a discrete approximation of Miller's integral (Korhonen et al., 2011; Miller, 1967):

$$\text{LAI}_e = 2 \sum_{i=1}^n -\ln(\bar{P}_i) \cos(\theta_i) w_i \quad (1)$$

where \bar{P}_i are ring-wise gap fractions as functions of zenith angle (θ) averaged across all photo sites at a given plot (Ryu, Nilson, et al., 2010) and w_i are weights corresponding to $\sin(\theta)d\theta$ of the midpoint angle of each zenith bin (Solberg, Næsset, Hanssen, & Christiansen, 2006).

2.3. LAI estimates from UFORE allometry

At the full set of 105 plots we identified and measured 612 trees following standard UFORE protocols. The crown measurements used by the UFORE model for estimation of leaf area include height of live top, crown base height, and average crown diameter. The log-linear allometric equation, initially created for full-crowned, deciduous, open-grown trees (Nowak, 1996) is:

$$\ln(LA) = -4.3309 + 0.2942L + 0.7312D + 5.7217S - 0.0148C + \epsilon \quad (2)$$

where LA is leaf area, L (crown length) is equal to the height of crown live top minus crown base height, D is the average crown diameter, S is a species-specific average shading factor, C is the crown's outer surface area represented by: $\pi D(L + D)/2$ and ϵ is an error term. Following back-transformation and correction for logarithmic bias, further adjustments may be made in cases of crowns with dimensions beyond the limits for which the equations were developed and for crowns that exhibit leaf loss due to factors such as dieback, defoliation and pruning

(D.J. Nowak, pers. comm., 2014). Plot level LAI estimates were computed by summing leaf area for all trees measured on the plot and then dividing by the total plot area of 408 m^2 .

2.4. Lidar data acquisition and processing

Waveform lidar data were collected in August of 2010 aboard a helicopter with a front-mounted Riegl Q560 laser scanner (Riegl USA, Orlando, Florida). The lidar data were georeferenced with two local differential GPS stations and stored in the UTM coordinate system (Zone 11 N, NAD83). The waveform was discretized using standard Riegl processing procedures to an average last-return point density of 22 points m^{-2} across the study area with additional returns (maximum of 4) available in tall vegetation. Height values on flat surfaces were evaluated to be precise to within 2 cm. Nominal scan angles ranged between 0 and 30° but the front-mounted sensor configuration resulted in a minimum pulse angle of 10° and a maximum of 30° . In this research the term pulse angle refers to the three dimensional, angular deviation from a theoretical pulse traveling perpendicularly to the ground. This is measured by constructing the 3-D line between a last return and a first return connected by their shared GPS time (Zhao & Popescu, 2009).

Each of the 71 plots was entirely sampled by at least two lidar flight lines and thus, in most cases, by multiple pulse angle distributions. Pulse angle was assigned to single echo pulses from multi-return neighbors in the same flight line or, in the absence of multiple returns, directly from the nominal scan angle. The point cloud was classified to ground, building, and vegetation using LAStools (LAStools v111216, <http://lastools.org>) with minimal adjustments to default settings and an overall classification accuracy, validated via manual image interpretation, exceeding 97%.

2.5. Plot-level estimates of LAI_e from lidar

We extracted 2.5, 5, 10, 11.4, 15, 20, and 25 m radius cylindrical subsets of the lidar point cloud centered at each hemiphoto site ($n = 243$) acquired across our set of 71 plots (methods workflow: Fig. 2). Hemiphotos and lidar pulses do not sample the same canopy (Morsdorf, Kotz, Meier, Itten, & Allgower, 2006; Richardson et al., 2009). The former is upward looking with a conical field-of-view while the latter is downward looking and results in a cylindrical extrusion of the field plot boundary. In an urban setting with highly variable canopy height, the

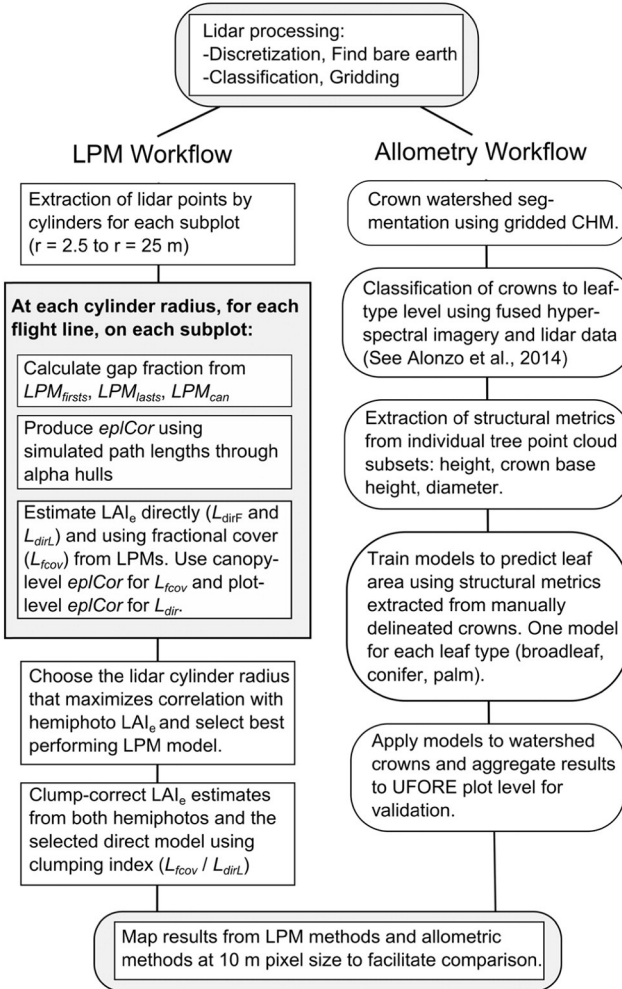


Fig. 2. Workflow diagram for both mapping approaches described in detail in the text. Please refer to Table 1 for full expansion of the acronyms in this figure.

ideal angular restriction of hemiphotograph view zenith and optimal sizing of the lidar cylinder radius is not known *a priori*. Thus, we extracted data at multiple radii in order to determine, on average, which cylinder size maximized the correlation between estimated LAI_e and the hemiphotograph LAI_e estimates that were produced from each of the five aforementioned zenith angle ranges.

2.5.1. Gap fraction from Laser Penetration Metrics

Accurate gap fraction estimation from LPMs is dependent on canopy gap size and arrangement, acquisition parameters such as beam footprint and scan angle, and the specific formulation of the LPM (Hopkinson et al., 2013; Morsdorf et al., 2008; Zhao & Popescu, 2009). We implemented three frequency-based LPMs as proxy measures of gap fraction (Table 1). The first two were calculated using all pulses extracted from a given plot (hereafter: “direct” method) and are adaptations of an LPM applied in a natural forest setting by Solberg et al. (2006) and a managed park setting by Richardson et al. (2009). Prior to correction for clumping (discussed in the following section), the direct method will yield significant overestimates of gap fraction whenever foliage is clumped among spatially disaggregated trees. However, this is likely similar to the overestimation produced from hemiphotograph analysis. We formulated the first LPM, simply as the inverse of fractional cover, only counting first returns, as follows:

$$\text{LPM}_{\text{firsts}} = 1 - \text{fCov} \quad (3)$$

Table 1
Key notation used throughout study.

Notation	Explanation
LPM	Laser Penetration Metric
LAI	Refers to “true” Leaf Area Index or Leaf Area Index from allometry
LAI_e	Effective Leaf Area Index
$\text{LPM}_{\text{firsts}}$	LPM gap fraction formulated only using first returns (all pulses on plot)
$\text{LPM}_{\text{lasts}}$	LPM gap fraction formulated with inclusion of last returns (all pulses on plot)
LPM_{can}	LPM gap fraction for canopy only (only includes pulses intersecting with canopy)
fCov	Plot canopy fractional cover
L_{dirF}	Plot-level, direct LAI_e using $\text{LPM}_{\text{firsts}}$
L_{dirL}	Plot-level, direct LAI_e using $\text{LPM}_{\text{lasts}}$
L_{fcov}	Plot-level LAI_e using LPM_{can} multiplied by fCov (used for clumping correction)
eplCor	Expected path length correction

Where:

$$\text{fCov} = \frac{F_c}{F_g + F_c} \quad (4)$$

In this model description, F denotes first and only returns, the subscript g is for ground, and subscript c is for canopy. When referring to lidar measurement from near overhead, there is no universally accepted differentiation between $1 - \text{fCov}$ and gap fraction. They may be considered equivalent (Hopkinson & Chasmer, 2009) or they may be distinguished in terms of the size of the gaps in question (Carlson & Ripley, 1997). To increase sensitivity to smaller gaps, gap fraction retaining last ground returns was calculated as the sum of first and last returns at ground level ($L_g + F_g$) divided by first ground, last ground, and first canopy returns:

$$\text{LPM}_{\text{lasts}} = \frac{L_g + F_g}{L_g + F_g + F_c} \quad (5)$$

A third LPM was calculated only in and under canopies as the ratio of ground last returns to the sum of ground last returns and first canopy returns:

$$\text{LPM}_{\text{can}} = \frac{L_g}{L_g + F_c} \quad (6)$$

This formulation does not include single returns that have penetrated through the canopy via larger gaps as these were accounted for in Eq. (4) for fractional cover. Logarithmic inversion of the direct measures, $\text{LPM}_{\text{firsts}}$ and $\text{LPM}_{\text{lasts}}$ will result in direct estimates of plot-level LAI_e . The same inversion of LPM_{can} will result in an estimate only of canopy LAI_e . This result must be rescaled by fCov in order to yield a comparable, plot-level result. In this study LAI_e from LPM_{can} was only used to correct the two direct estimates, as well as hemiphotograph-estimated LAI_e , for plot-scale clumping. To evaluate whether these metrics may be implemented with more commonly available lidar datasets, each LPM was additionally calculated for decimated pulse densities of 5 pts m^{-2} and 2 pts m^{-2} .

2.5.2. Pulse interception simulation for path length and clumping correction

Gap fraction estimates from LPMs will vary as a function of path length through the canopy. This component of variability is commonly mitigated through retention only of pulses with near-nadir scan angles (e.g., Morsdorf et al., 2008) but has also been accounted for using a cosine correction, which effectively normalizes path length by pulse angle (e.g., Zhao & Popescu, 2009). Relying on narrow swaths of data in cities is problematic if we hope to operationalize spatially extensive LAI_e measurements at reasonable cost. However, the application of a simple cosine correction (e.g., $1/\cos(\Theta)$ where Θ = pulse angle) may be inappropriate in areas of discontinuous canopy and variable crown

morphology (Holmgren et al., 2003). Pulse angles in this study's lidar dataset were never less than 10 degrees off-nadir. Thus, in furtherance of objective #2, we simulated canopy pulse interception through a range of pulse angles and crown geometries to develop a more precise method for correction called *expected path length correction* (*eplCor*). Simulator detail and code are available in the electronic supplementary materials. Portions of this MATLAB-based (vR2013b, The MathWorks, Inc.) simulator code were also used for the "on-the-fly" simulation using the lidar data referenced in the following section.

eplCor is the ratio of the expected pulse path length through the crown at a given pulse angle and crown geometry compared to the hypothetical, simulated nadir path length. *eplCor* is assessed at the canopy level by comparing the path lengths only of pulses intersecting the crown's alpha hull. Alpha hulls differ from convex hulls in that the requirement of convexity is relaxed when the user-defined alpha scale parameter is finite. Use of alpha hulls allows for more precise wrapping of a set of spatially disaggregated crowns. At the plot level, all plot pulses are included to account for the fact that, with upright crown geometry, as pulse angle increases, more pulses will pass through the crown. We examined the relationship between pulse angle and LAI_e for upright, intermediate, and spreading geometries based, respectively, on 75th, 50th, and 25th percentile height-to-diameter ratios of our 612 field-measured trees. Results are reported as "simulated LAI_e " (SLAI_e) and produced from equations following the form of Eq. (7) for plot-level estimates and Eq. (9) for canopy-level estimates rescaled by $f\text{Cov}$ (see Section 2.5.3).

The extent to which estimates of LAI_e will underestimate true LAI due to clumping is also partially determined by urban forest stand configuration. In an urban setting characterized by isolated trees, clumping of foliage occurs at the shoot, branch, and plot scales. While the error from clumping is presumed to be the same for both lidar and hemiphotograph estimates, we believe that tree spacing in our urban study area will lead to underestimates that may be too large to ignore. Here, we again used pulse interception simulation to examine how the distribution of foliage throughout a plot, from highly clumped (e.g., aggregated in a single, dense palm) to fully random, drives underestimates of direct LAI_e measures. To accomplish this, we set true plot LAI to values ranging from 0.11 to 1.67. At each value we varied the radius of a simulated tree, and thus the foliage density, from 3 m to 15 m. To produce a clumping ratio we divided simulated LAI_e calculated using Eq. (9) by simulated LAI_e calculated using Eq. (7) (See Section 2.5.3). This ratio presumes that a plot-level estimate of LAI_e made by first measuring only canopy LAI_e and then rescaling by $f\text{Cov}$ will not be impacted by the spacing / arrangement of the plot's trees (Ryu, Nilson, et al., 2010).

2.5.3. Estimating LAI_e from lidar data

For each cylinder radius, at each hemiphotograph site, for each flight line, LAI_e was calculated from lidar data directly at the plot level using only first returns (L_{dirF} , where the subscript *F* indicates first returns) and including last returns (L_{dirL} where the subscript *L* indicates last returns) as well as indirectly from canopy LAI_e multiplied by $f\text{Cov}$ (L_{fcov}). Formulations:

$$L_{dirF} = \frac{-\ln(LPM_{firsts})}{k \cdot eplCor} \quad (7)$$

$$L_{dirL} = \frac{-\ln(LPM_{lasts})}{k \cdot eplCor} \quad (8)$$

$$L_{fcov} = \frac{-\ln(LPM_{can})}{k \cdot eplCor} \cdot f\text{Cov} \quad (9)$$

where LPM_x is the relevant gap fraction generated using the LPM Eqs. (3), (5) and (6). We set $k = 0.5$ to correspond with the commonly reported spherical leaf angle distribution (LAD) for leaves of any size (Chen et al., 1997). Given the high species diversity in our study area

there was little basis on which to choose any LAD other than spherical. We also report k as estimated using weighted linear regression and a no-intercept model to evaluate the deviation from this expected value (e.g., Solberg et al., 2006). Linear regression weighted by lidar-estimated LAI_e was selected in order to account for increasing error variance at higher values of LAI_e . Coefficients of determination were calculated based on sums of squared error and total sums of squares for the untransformed data relative to the weighted least squares fit. For the airborne lidar data, *eplCor* was estimated using on-the-fly simulation. That is, for each of the 243 subplots, an alpha hull was generated for canopy returns and expected path lengths were calculated based on median pulse angle, median pulse azimuth, and crown geometry. The flight line results, weighted by number of pulses, were averaged back to the full plot ($n = 71$) level. Clumping ratios were calculated and multiplied through L_{dirF} , L_{dirL} and the hemiphotograph LAI_e results to account for plot-scale clumping.

2.6. Crown scale estimates of LAI using lidar-measured crown dimensions

Objective #3 of this study was to map LAI at the crown scale using allometric methods. Note: This study does not use LAI_e and LAI interchangeably. The latter metric represents an estimate of "true" LAI that is neither impacted by foliar clumping nor commingling of woody and leafy plant materials. The choice to forgo LPM methods in favor of allometry for mapping LAI at the crown scale is warranted for several reasons: 1) Currently, allometric estimation using the UFORE model is the most common means for estimating LAI in US cities; 2) LPMs can only be used when it is possible to tally the full set of ground-reflected pulses that have passed through a given tree crown. This is difficult with highly off-nadir pulse angles where the (X,Y) positions of ground returns are displaced significantly with respect to the (X,Y) positions of canopy returns; 3) Even with high-point density and low flight altitude, individual tree crowns with high LAI may not allow passage of any pulses, resulting in numerical overflow of the gap fraction inversion computation; 4) Objective #4 of this study was to compare the results of mapping methods with distinct theoretical underpinnings.

The following sections describe in detail how we used lidar to estimate the same structural inputs that are used in the UFORE allometric equation (Eq. 2) and then how we applied the results to all crowns in our study area (Fig. 2).

2.6.1. Crown segmentation and leaf type classification

The allometric Eq. (2) used in UFORE to estimate leaf area from crown dimensions also incorporates a species-specific shading factor. This factor is included to account for the large species-driven variation in leaf size, shape, and arrangement that may be encountered within any measured crown volume. In this study it was not feasible to develop coefficients for each species due to limited training data. Instead we classified each tree to the leaf-type level (i.e., broadleaf, needleleaf, palm). Segmentation of canopy into individual crowns and leaf-type classification was undertaken prior to beginning this study. The process is detailed in Alonso, Bookhagen, and Roberts (2014). A brief synopsis follows:

Canopy segmentation made use of the marker-controlled watershed algorithm on a gridded lidar canopy height model in the manner originally proposed by (Chen, Baldocchi, Gong, & Kelly, 2006). Spectral data from the Airborne Visible/Infrared Imaging Spectrometer (AVIRIS, Green et al., 1998) and structural metrics (e.g., height, height-to-width ratios, porosity) were extracted from each crown and fused. Classification of 29 common species was carried out on the fused dataset using canonical discriminant analysis to 83.4% overall accuracy. Classification of all crown segments to the leaf-type level was carried out with 93.5% accuracy. This classification information was used in Section 2.6.3 to facilitate the formulation of separate leaf area models, one for each leaf type.

2.6.2. Measurement of crown dimensions from the lidar point cloud

In this study, tree height and crown base height were estimated directly from the 3-D lidar point cloud by first finding the vertical midpoint between the highest and lowest return in a given segment that was classified as canopy. From the midpoint, a 0.25 m window was moved vertically up and down the tree, stopping when the slice contained fewer than a predetermined minimum number of returns. This method proved superior to a quantile-based method because of the significant presence of cultivated shrubbery below the crown (Fig. 3a) and power lines or branches of neighboring trees above (Fig. 3b). Average crown diameter was calculated from watershed crown area after abstracting each segment to its circle of equivalent area. These measurements served as the raw inputs to Eq. (2).

2.6.3. Model formulation using crown measurements from manually delineated crowns

As in the UFORE model, total leaf area was estimated as a precursor to LAI. We trained the lidar model to predict leaf area using 109 manually delineated crowns with known leaf type and leaf area. We used a log-log adaption of Eq. (2) due to the lognormal frequency distributions of each independent variable, the lognormal distribution of leaf area, and clear non-linear, bivariate relationships between each predictor and response:

$$\ln(LA) = \ln(b_0 + b_1 \cdot L + b_2 \cdot D + b_3 \cdot C) \quad (10)$$

where LA is leaf area, L is crown length, D is average crown diameter, C is crown surface area, and b_x are empirically determined coefficients. Coefficient estimation was carried out on both the pooled set of 109 crowns and the sets separated by leaf type using weighted least squares regression.

2.6.4. Model application on watershed crowns

The models formulated using manual crowns were applied to all watershed segments in the study area after estimating the crown dimensions for each segment. Following segment-level estimates of leaf area, LAI was calculated at the field-plot level to allow for accuracy assessment against aggregated UFORE values. To clarify: it is not possible to validate individual crown results for watershed segments because it is not known whether a segment contains only a part of one, exactly one, or more than one tree. Thus, the leaf area estimates for the 1584 watershed crowns that intersected 71 UFORE plots were summed by plot and divided by the plot area (408 m^2) to yield plot-level LAI.

2.6.5. Map making and model intercomparison

A study-area wide map of LAI_e was generated at 10 m pixel resolution using the best performing of the L_{dirt} and L_{dirt} models. Finer resolution was not considered because it has been previously shown in an

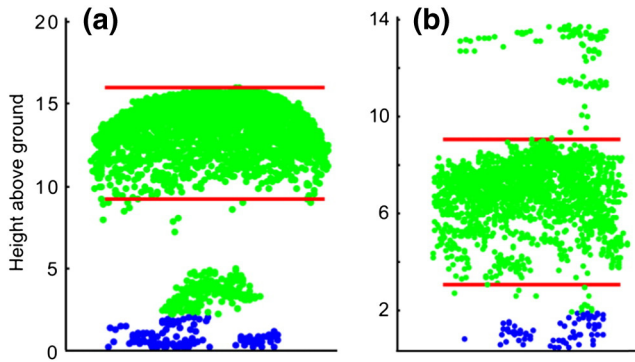


Fig. 3. Two example crowns based on airborne lidar data collected during August 2010 with automatically estimated height and crown base height (red lines). Green dots indicate returns classified as canopy. (a) Presence of understory shrubbery. (b) Crown is overhung by power lines.

urban setting that, even with high pulse density, pixel sizes of 3 m led to data gaps due to lack of ground returns (Richardson et al., 2009). Moreover, given our study's mean pulse angle (20°) and mean canopy height (10 m) the horizontal displacement of ground returns relative to canopy returns was expected to exceed 50% of all pulses if 5 m pixels were generated. No such limitation existed for the allometric outputs which were mapped at the crown scale. The crown scale map was subsequently gridded to 10 m pixels through intersection and reapportionment operations in a GIS to allow for spatially explicit comparison with the selected LAI_e result. We compared the model results for the 71 study plots and also throughout a spatial subset of the study area using 450 randomly distributed sample points. Additionally, we compared all possible pairwise relationships ($n = 12$ when each ground and each lidar method is used as an independent and a dependent variable) to establish rough error bounds on LAI mapping in cities. For purposes of intercomparison, we report root-mean squared error (RMSE) and slope coefficient values from weighted least squares regression with inclusion of an intercept term in all cases.

3. Results

3.1. Comparison of ground-based estimates

Hemiphot LAI_e and allometrically determined LAI from UFORE field measurements have different theoretical underpinnings. Nevertheless, there was a significant linear relationship between Hemiphot LAI_e and UFORE allometric LAI ($r^2 = 0.53$), although the slope of 0.34 indicated that hemiphot LAI_e was generally lower than allometric LAI (Fig. 4). This relationship and all other linear relationships reported in this research were significant at the $p = 0.001$ level.

3.2. Plot fractional cover

Fractional cover was calculated for each plot using Eq. (4) and it was compared to field estimates made using UFORE protocols. There was a significant linear relationship between the two estimates of fractional cover (r^2 of 0.85, $y = 0.86x - 0.92$, data not shown), with lidar estimates generally resulting in 5–10% more fractional cover. The lidar results may be more accurate than the UFORE measurements because the latter produce relatively coarse estimates by dividing the sky into 4 quadrants and estimating the canopy cover in each visually.

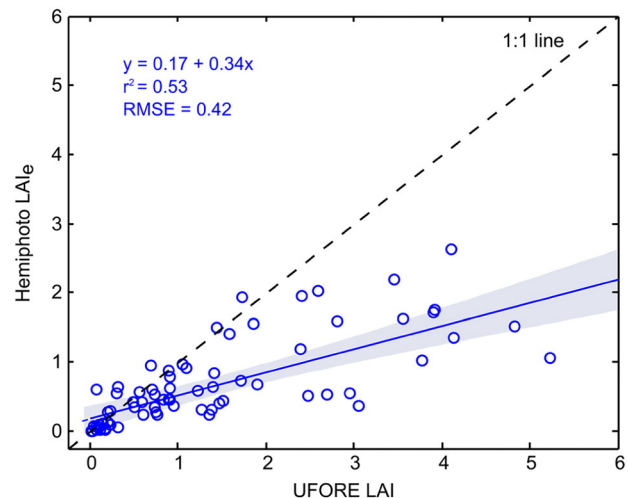


Fig. 4. The relationship between UFORE allometric LAI from field measurements and hemiphot derived LAI_e. Grey shading in this and all similar plots indicates the 95% confidence interval of the regression equation.

3.3. Correcting for path length and plot-scale clumping using simulation

The expected path length correction method was evaluated in our simulation environment to determine its robustness with respect to crown geometry and distribution of foliage (Fig. 5). LAI_e was underestimated for all crown geometries at both the canopy and plot levels with underestimation exacerbated by increased pulse angle, particularly for the upright and intermediate crowns. At the canopy level, for upright crowns, *eplCor* strongly compensated for the underestimation at pulse angles >5°. At 30° off nadir, the LAI estimate was corrected from 1.65 to 2.48. For the intermediate crown, the correction at 30° raised the LAI estimate from 1.98 to 2.38. Due to minimal change in pulse-angle dependent path length in the spreading crown, *eplCor* had negligible impact. Simulated plot level results based on rescaled canopy LAI_e mimicked the patterns produced in the canopy level results as they only differ by the scalar, *fCov*. In the case of the direct, plot-level results however, the net effect of *eplCor* (with non-canopy pulses now included) was to lower the estimated LAI_e by implicitly compensating for the higher number of pulses making contact with canopy at higher pulse angles.

Simulation of plot-scale clumping showed that underestimates of true plot LAI varied as a function of foliage density (the ratio of crown projection area to plot area) and LAI (Supplementary Material Fig. S1). Underestimates were most severe when true plot LAI was highest (1.67) and the foliage density was highest (canopy radius = 3 m, plot radius = 15 m). In this case, the measured LAI value was only 5% of

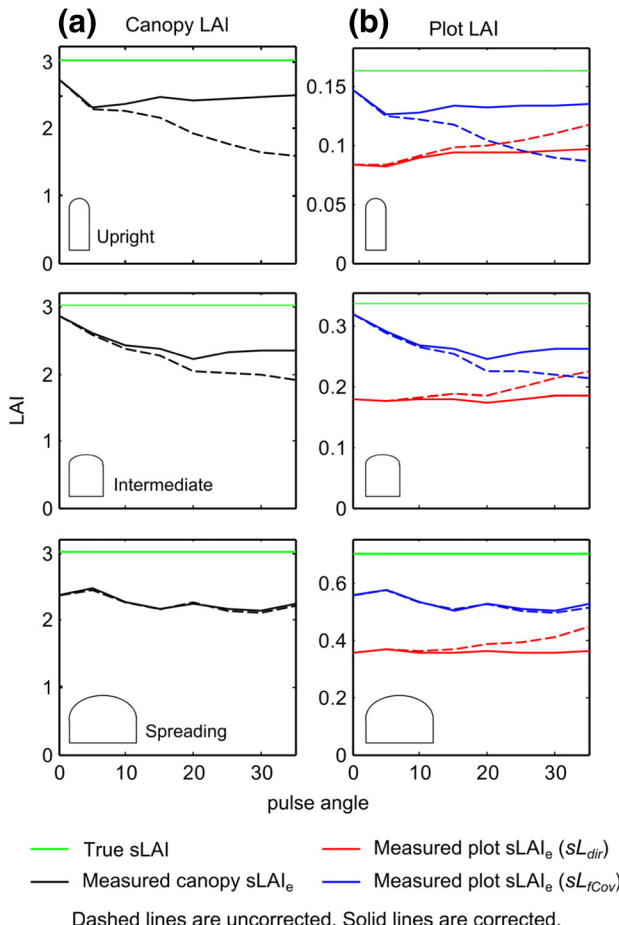


Fig. 5. Adjustments to simulated LAI_e (sLAI_e) using expected path length: (a) Canopy-level adjustment including only pulses intersecting the alpha hulls. (b) Plot level adjustments including all plot pulses in *eplCor* calculation. *sL_{dir}* uses the “direct” method (Eq. (8)), *sL_{fCov}* uses the “canopy method” (Eq. (9)). Upright, intermediate, and spreading crowns defined as 75th, 50th, and 25th percentile height-to-diameter ratios of field-measured trees.

true LAI. As foliage became more evenly distributed, estimates improved, following a logarithmic trajectory whose coefficients varied with true plot LAI. For instance, for a true plot LAI of 0.66, with all canopy clumped into a tree with a radius of 7 m, measurement yielded an LAI value that was 45% of true LAI. At a true plot LAI of 0.22 with foliage fully distributed throughout the 15 m radius plot, the measured LAI value was 90% of true LAI.

3.4. Plot LAI_e estimates from lidar data

On the assumption that view geometry alignment does not depend on LPM formulation, LAI_e was directly estimated using only *L_{dirL}* at all plot radii and all hemiphoton zenith bins with Eq. (8). The coefficient of determination was maximized for *L_{dirL}* using the range of hemiphoton zenith angles from 0 to 45° and a cylinder radius of 10 m (Fig. 6). This correlation theoretically indicates a mean canopy height between 10 and 20 m, which indeed bounds the mean height of field-measured canopy: 12 m. This optimal zenith bin and lidar data cylinder radius was used in all further analyses.

Model performance of *L_{dirF}* (first returns only) and *L_{dirL}* (inclusion of ground last returns) was assessed by simultaneous minimization of bias and maximization of the coefficient of determination with respect to hemiphoton LAI_e. After multiplication by the clumping ratio, the best model performance was exhibited by *L_{dirL}* with a no-intercept linear relationship of $y = 0.99x$, $r^2 = 0.82$, and RMSE = 0.41 (Fig. 7). Examination of *L_{dirF}* ($y = 0.73x$, $r^2 = 0.73$, RMSE = 0.40) showed a linear relationship with hemiphoton LAI_e at lower values. At higher hemiphoton LAI_e values, significant overestimates were present. For simplicity, only *L_{dirL}* was considered for subsequent analyses. Changes to slope, r^2 , and RMSE values after decimation to 5 pts m^{-2} were each within 1% of the full point-cloud values reported above. After decimation to 2 pts m^{-2} , the *L_{dirL}* slope decreased to 0.98, RMSE increased from 0.41 to 0.42 and the r^2 value decreased from 0.82 to 0.80. *L_{dirF}* slope decreased from 0.73 to 0.72, RMSE increased from 0.40 to 0.42 and r^2 decreased from 0.73 to 0.69.

Canopy-level *eplCor* was applied to correct the *L_{fCov}* model, while the plot-level analog was applied to correct the estimates from *L_{dirL}* (Fig. 8). These plot-level corrections resulted in an 8% reduction in bias and a change in slope from 0.92 to 0.99. The canopy level correction, after conversion to a comparable plot-level result, resulted in a 1% increase in bias with a decrease in slope from 0.74 to 0.73. This latter result is merely presented to show the effect of *eplCor*. We do not believe that the hemiphoton dataset offers comparability with *L_{fCov}* results due to different sensitivities to clumping. The mean value of the clumping ratio

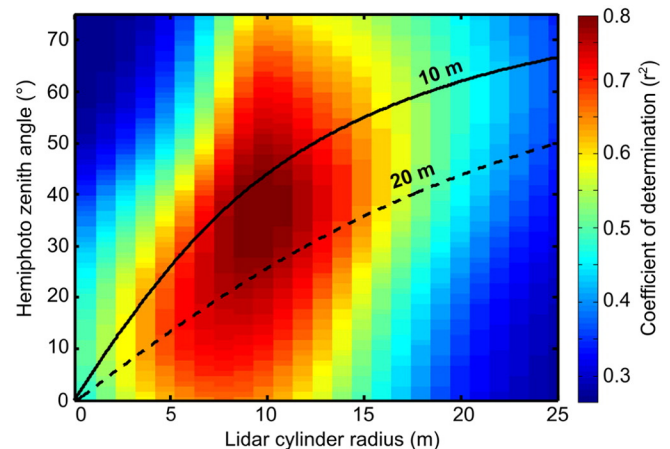


Fig. 6. Coefficient of determination (r^2) matrix for the relationship between LAI_e from hemiphotons and LAI_e using lidar and the *L_{dirL}* model. Theoretical lines of maximum correlation for 10 m and 20 m canopy height are also displayed.

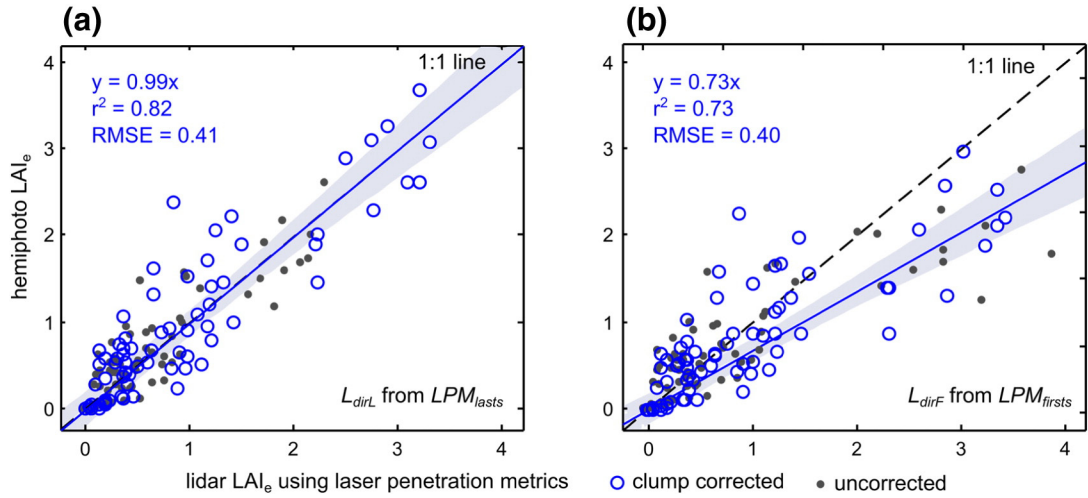


Fig. 7. Weighted, no-intercept, linear relationships between hemiphot LAI_e and LAI_e predicted using model L_{dirL} (a) and L_{dirF} (b). Clump-corrected results shown in blue and uncorrected result shown in gray. Results only displayed for full point cloud without decimation.

(L_{fcov}/L_{dirL}) was 1.4 (standard deviation = 0.26), which indicates similarity to the simulated values of 1.43, 1.42, and 1.49 for the upright, intermediate, and spreading crowns, respectively.

3.5. LAI estimates using lidar-measured crown dimensions and allometry

There was strong agreement between crown diameter, crown length, and crown-surface area calculated from lidar and their field-measured analogs, with r^2 values of 0.95, 0.87, and 0.94 respectively (Fig. 9). Log-log fits by leaf type were established between the lidar structural measurements and the UFORE measurements:

$$\ln(LA_b) = \ln(1.76 + 0.60L_b + 2.32D_b - 0.44C_b) \quad (11)$$

$$\ln(LA_c) = \ln(-5.05 - 2.06L_c - 5.38D_c + 4.90C_c) \quad (12)$$

$$\ln(LA_p) = \ln(7.02 + 2.11L_p + 11.09D_p - 5.33C_p) \quad (13)$$

where the subscripts *b*, *c*, and *p* denote broadleaf, needleleaf, and palm leaf types respectively. Formulation of separate log models for each leaf type resulted in an r^2 value of 0.87 (RMSE = 0.39) compared to $r^2 = 0.78$ (RMSE = 0.48) for a combined model.

Application of the above models to the set of watershed segments intersecting our UFORE field plots ($n_{segs} = 1584$) resulted in an overall r^2 of 0.84 and a slight overall underestimate ($y = 0.97x + 0.10$, RMSE = 0.53) compared to LAI estimated from field data using the native UFORE model equations (Fig. 10). At the watershed-crown level, combined model $r^2 = 0.81$ (RMSE = 0.57, data not shown).

3.5.1. Comparing the lidar models and mapping the estimates

There was strong agreement ($r^2 = 0.86$, $y = 0.05 + 1.22x$, RMSE = 0.59) between the LAI_e results from the L_{dirL} model and LAI measured allometrically using lidar-extracted crown measurements. Allometric LAI was underestimated slightly by L_{dirL} possibly, in part, because the latter does not account for shoot/branch scale clumping and because penetration metrics are prone to saturation at high LAI. All ground-based and lidar models were related with root-mean squared errors ranging between 0.39 and 0.93 and slope values between 0.45 and 1.21 (Table 2).

Maps were generated using each of the models and are displayed here, for the purposes of visual clarity, as spatially corresponding subsets of the full study area (Fig. 11). While produced initially at different spatial resolutions (10 m pixels for LAI_e versus crown scale for lidar allometry), the broad scale similarities are visually apparent. After

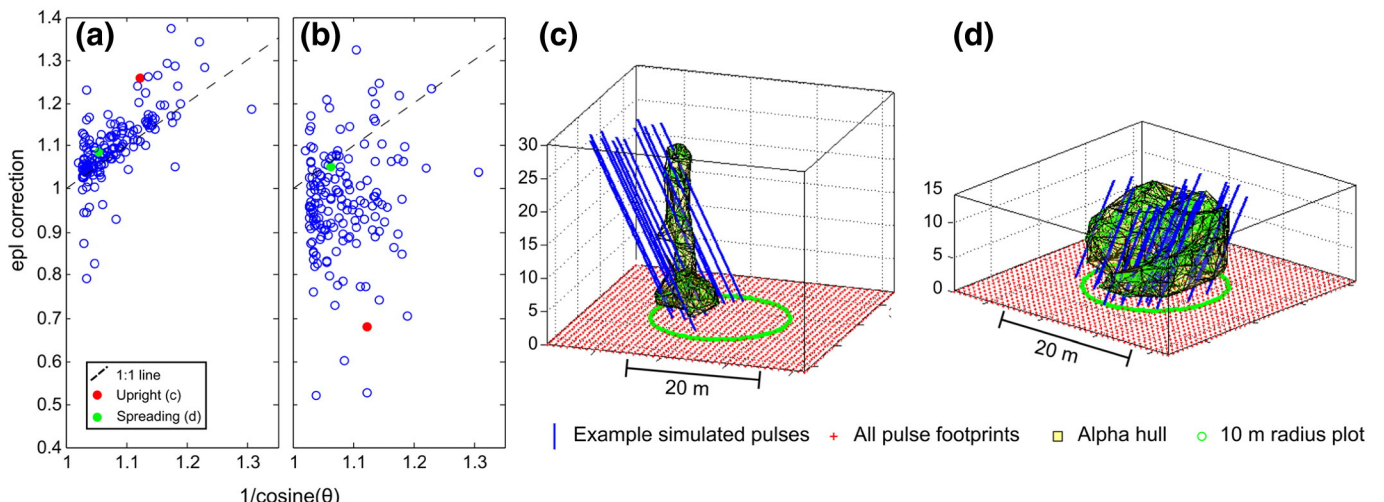


Fig. 8. Demonstration of expected path length correction (eplCor) at plot and canopy levels. (a) Plot level correction compared to cosine correction. (b) Canopy-level correction compared to cosine correction. (c) Example of alpha hull wrapping a clump of upright palm trees. (d) An alpha hull wrapping a closed canopy of spreading oak trees.

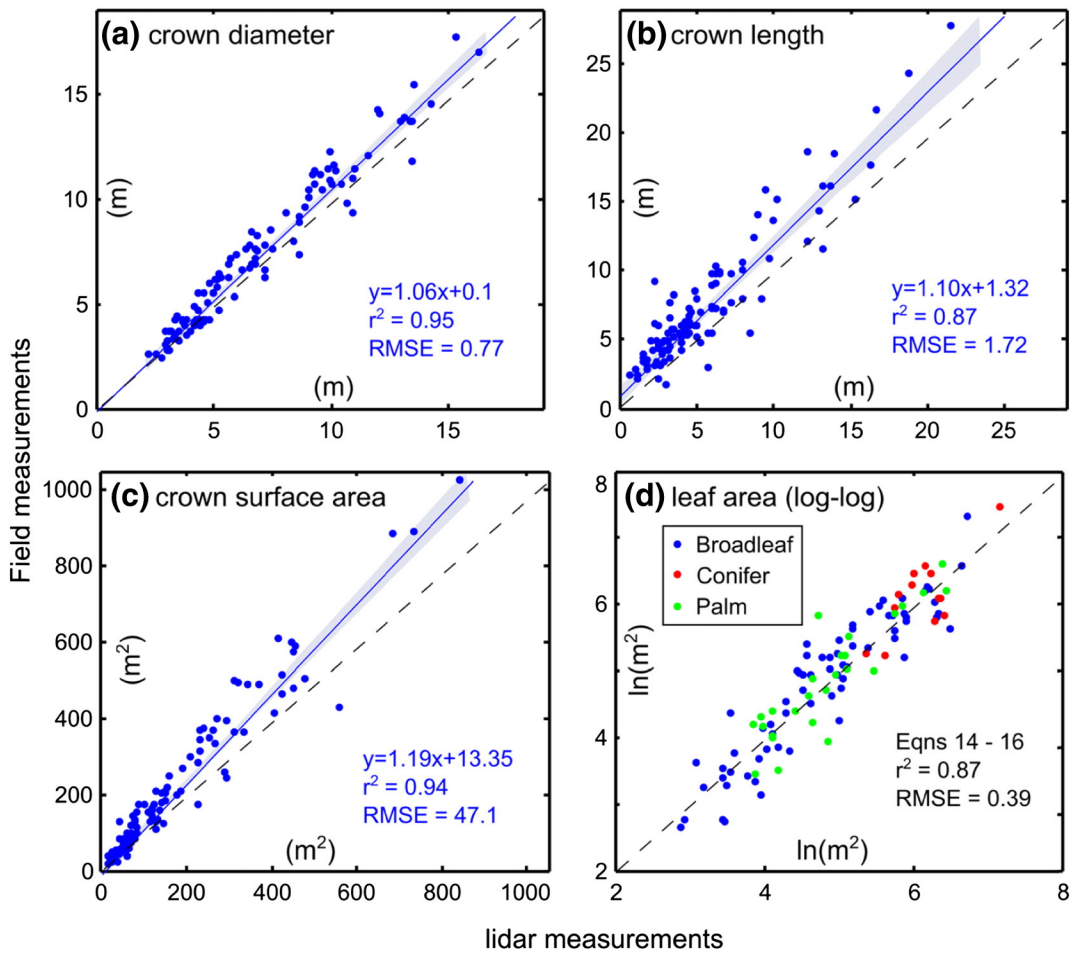


Fig. 9. (a)-(c) Relationship between field-measured crown dimensions and the same measurements made using airborne lidar on 109 manually-delineated crowns. (d) Log-log fit of lidar-predicted leaf area and leaf area estimated from crown measurements in the field.

resampling the crown-level map to 10 m resolution, we assessed the patterns of disagreement between the two methods (Fig. 11c). As anticipated based on plot-level results, the allometric model generally produced higher estimates. The L_{dirL} model produced higher LAI_e values

mostly under large broadleaf canopies as illustrated in the inset map. To compare the maps more rigorously, we extracted pixel values from each 10 m map at 450 points. Map agreement between the two models yielded a coefficient of determination of 0.72. Interestingly, the bias in the map was the opposite of the bias in the plot-level comparison (0.78 instead of 1.22). In the map, at high LAI, L_{dirL} produced higher values. This may be due to the higher likelihood of 10 m pixels being under closed, broadleaf canopy compared to the 20 m diameter sample plots.

4. Discussion

4.1. Mapping LAI_e with laser penetration metrics (objective #1)

We found strong agreement between LAI_e estimated from hemiphotograph fraction inversion and LAI_e estimated using LPMs, as has been previously reported for natural forests (Hopkinson & Chasmer, 2009; Richardson et al., 2009; Solberg et al., 2006, 2009; Zhao & Popescu, 2009). Our best result ($r^2 = 0.82$, $y = 0.99x$, RMSE = 0.41) comparing LPM methods to hemiphotographs was produced with the L_{dirL} model. We found that the inclusion of ground last returns (LPM_{lasts}) in our LPM formulation was necessary to retain model sensitivity at $LAI_e > 2$ (Fig. 7a). This was due to the fact that, at $LAI > 2$, LPM_{firsts} was insensitive to change in gap fraction because the beam footprint was larger than the typical gap size (Lovell, Jupp, Culvenor, & Coops, 2003; Solberg et al., 2009). For low canopy cover plots either metric is likely sufficient because LAI_e is largely governed by fractional cover. In regions of partial vegetation cover specifying LAI may be redundant if fractional cover is

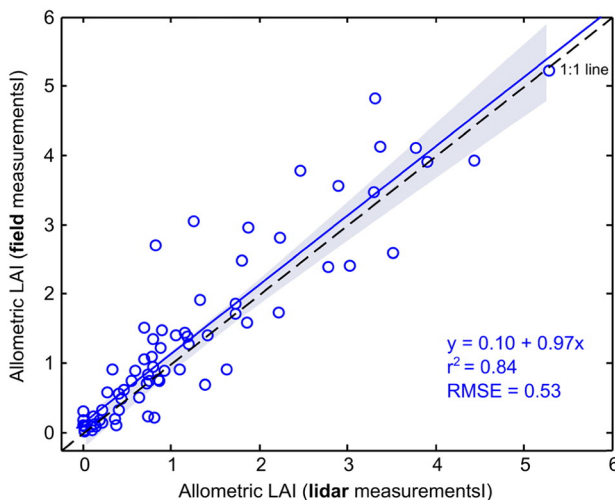


Fig. 10. Allometric LAI from field measurements predicted by allometric LAI from lidar structural measurements using separate models for each leaf type (Eqs. 11–13). Aggregation of individual crown estimates to the field plot scale.

Table 2

Weighted Least Squares root mean squared error (bold) and slope coefficients (in parentheses) for all combinations of field and lidar-estimated LAI or LAI_e . For comparability, all table entries are based on WLS regression with inclusion of an intercept term.

		Dependent Variable			
		UFORE	Hemiphoto	Lidar LPM	Lidar allom.
Independent variable	UFORE	-	0.42 (0.45)	0.57 (0.53)	0.48 (0.87)
	hemiphoto	0.93 (0.95)	-	0.39 (0.89)	0.74 (0.94)
	lidar LPM	0.86 (0.89)	0.4 (1.10)	-	0.59 (1.21)
	lidar allm.	0.53 (0.97)	0.56 (0.69)	0.44 (0.71)	-

already known (Carlson & Ripley, 1997). Still, it is unclear whether L_{dirF} leads to under- or overestimation of LAI_e as it is unknown whether we are more likely to digitize canopy returns where the pulse did not fully intersect with canopy or ground returns where part of the pulse did intersect with canopy (Hopkinson & Chasmer, 2009). The addition

of last returns, beyond allowing for greater sensitivity to smaller gap sizes, increases the effective pulse density, which raises the likelihood that under- and overestimates at gap margins will cancel out.

In L_{fcov} only last returns on the ground were accounted for in the numerator. Thus, in dense canopy, the penetration rate may be zero,

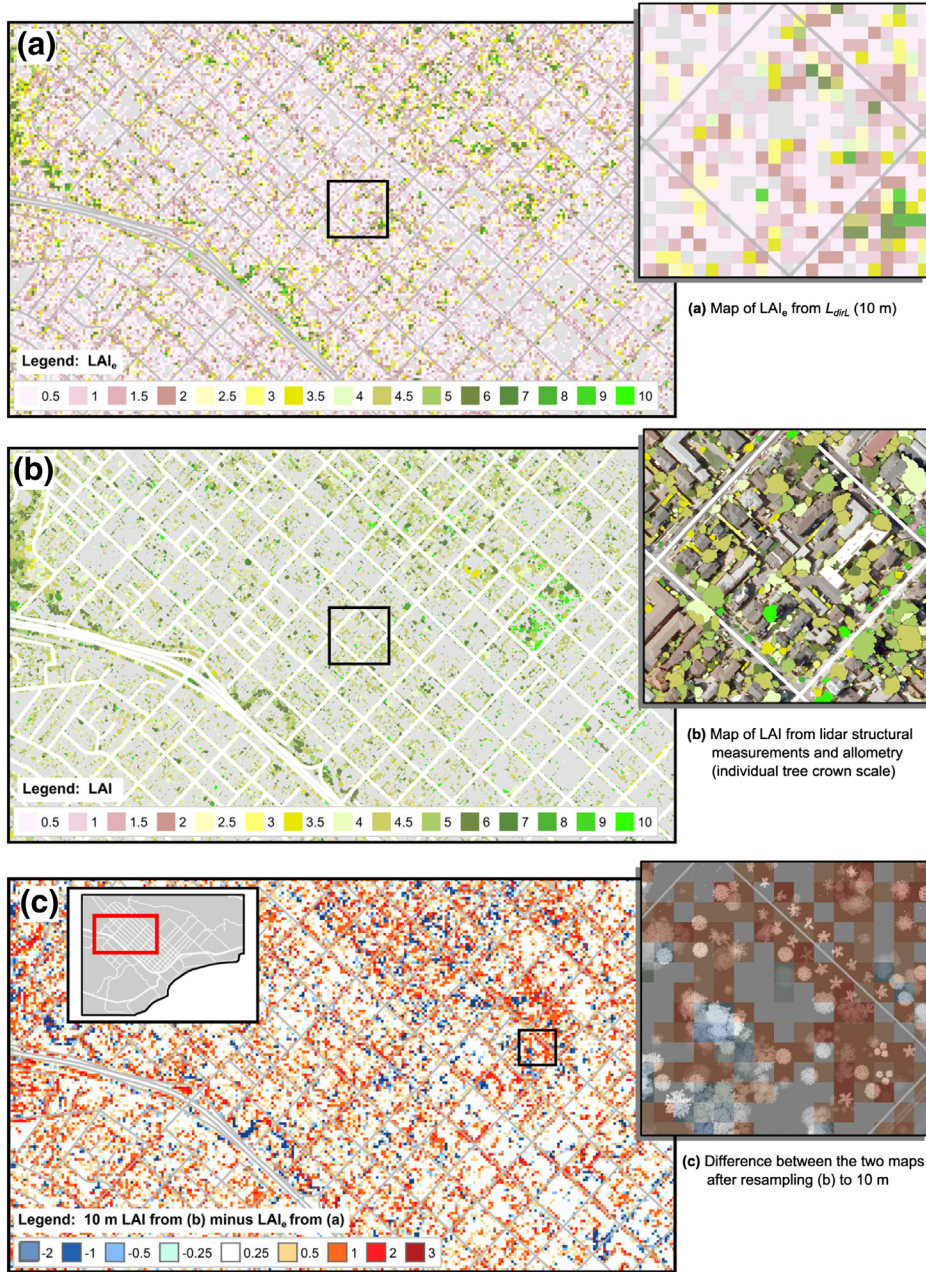


Fig. 11. (a) Map of LAI_e using the L_{dirL} model at 10 m pixel size for downtown Santa Barbara (see map inset for location). (b) Map of LAI from lidar extracted structural metrics and allometry at individual crown scale. (c) The L_{dirL} map subtracted from the allometric map after the latter was resampled to 10 m resolution. All legends are numbered with the class' highest value.

resulting in an LAI_e of infinity. This did not occur on our 71 plots because their 20 m diameter and relatively sparse canopy always allowed for some ground returns. However, on 73 out of 41,134 (0.2%) of our 10 m grid squares this numerical overflow forced exclusion of the L_{fcov} values. While this failure rate was low, it would increase at smaller pixel sizes and when applying a penetration metric to dense, individual crowns. Canopy density is only one cause of this error: For either individual crowns or small pixels, ground returns from non-nadir pulses will exhibit horizontal displacement with respect to associated canopy hits. The number of ground returns that should be associated with the pixel in question, but are actually counted in an adjacent pixel, will vary as a function of pixel size, canopy height, and pulse angle.

While it was necessary to include last returns in order to maintain model sensitivity at higher LAI_e , sensitivity was not impacted significantly through reduction in pulse density. The full point-cloud relationships depicted in Fig. 7a, differed negligibly in terms of r^2 and bias from those generated at 2 pts m^{-2} . The only noteworthy deviation occurred with 2 pts m^{-2} sampling density in plots with very low fractional cover. In several of these cases higher pulse density was required in order to detect the presence of small patches of vegetation. In high cover plots, the low pulse density was still sufficient, at least at 10 m radius plot scale, to produce similar ratios of ground returns to all returns. The fact that this method may be successful at lower pulse densities allows cities to consider similar analyses with existing lidar datasets.

4.1.1. Correcting for off-nadir pulse angles and clumping (objective #2)

Assessment of LAI_e using Beer-Lambert's law assumes that attenuation of light through the canopy is partially a product of its passage through N statistically independent horizontal layers of canopy (Jonckheere et al., 2004). When the N layers are sufficiently thin and foliage is distributed randomly, the probability of light interception in a given layer follows a Poisson distribution. For measurement of LAI_e from overhead lidar, we assume that this passage follows a near vertical path from sensor to ground. If, however, the pulse angle deviates significantly from 0° , we must consider how this change affects the path length of the pulse through the canopy. All else being equal, an increase in path length due to sensor positioning relative to a crown will lead to a spurious reduction in gap fraction. Given a continuous, uniform extent of canopy, it is reasonable to assume that path length correction can be applied in the form of $1/\cos(\Theta)$ where Θ is the angular deviation from nadir.

Our urban study area, however, was characterized by heterogeneous canopy such that path length was additionally dependent on crown geometry and pulse azimuth. We found that, at the canopy level, a simple cosine correction had little relationship with *eplCor* and, under most circumstances, prescribed an adjustment that erroneously lowered the LAI_e estimate (Fig. 8b). This effect can be seen clearly with the cluster of highly upright palms shown in Fig. 8c. At the plot level, however, the utility of the cosine correction remained largely intact (Fig. 8a). On plots dominated by spreading crowns (Fig. 8d) the distinction between plot and canopy-level correction is less pronounced. At the plot level there is a coherent linear relationship between *eplCor* and simple cosine correction (Fig. 8a). Thus, it is not surprising that this use of *eplCor* only resulted in a 2% improvement over $1/\cos(\Theta)$. The true value of *eplCor* will more likely be realized should measurement of LAI_e become feasible at the individual crown scale.

Estimation of true LAI from hemiphotos requires a horizontally continuous, random distribution of foliage across all view zenith and azimuth angles as well as the ability to separate woody plant matter from photosynthetic material (Jonckheere et al., 2004). The same requirements apply to plot-level estimation using lidar. While difficult to discern from the literature, there appear to be a number of studies that utilize hemiphotos under discontinuous canopy conditions (e.g., Richardson et al., 2009; Solberg et al., 2006; Zhao & Popescu, 2009). Under these conditions, estimating LAI_e is still possible (and technically valid) but the magnitude of the departure from true LAI

may become extreme due to significant spatial separation among clumps of foliage. Given the extremely discontinuous canopy in a semi-arid, urban environment, we attempted to account for clumping attributable to tree spacing.

We measured clumping as the ratio of LAI_e estimated using L_{fcov} to L_{dirL} and produced an average clump ratio value of 1.4 for our study area. We multiplied both the hemiphoto LAI_e estimates and the L_{dirL} estimates by the plot-specific clump ratio. This result cannot be validated directly but we did find increased agreement with allometric results, which could indicate that the correction for plot-scale clumping shifts LAI_e values somewhat closer to true LAI. It may behoove future researchers to experiment with ground-based methods that allow for indirect LAI_e estimation of individual trees or coherent canopy clumps. Methods of this type that have been used in sparse canopy conditions include non-hemispherical digital canopy photography (Pekin & Macfarlane, 2009; Peper & McPherson, 2003; Ryu, Sonnentag, et al., 2010) and the LAI-2000 with restrictions placed on the view zenith and azimuth (Peters & McFadden, 2010).

4.1.2. Leaf angle distribution

We used a fixed value of $k = 0.5$ for all LAI_e models because it represents the extinction coefficient for the spherical leaf angle distribution (LAD). In the least squares fit between L_{dirL} and hemiphoto LAI_e , our estimated slope coefficient was 0.99. This equates to a modeled k value of 0.495, suggesting that in a highly mixed urban forest, an initial k value of 0.5 is reasonable. This is consistent with Richardson et al. (2009), who estimated $k = 0.485$ in a semi-urban park setting with a mix of broadleaf and needleleaf species. Falster and Westoby (2003) digitized the LADs in three dimensions of 38 perennial species in sclerophyll woodland qualitatively similar to the oak/eucalypt assemblages common in southern California. They found that each species had a unimodal LAD with mean leaf angles ranging from 27° (planophile) to 74° (erectophile). Across their entire sample, the cross-species mean leaf angle was 52° which is approximately equidistant from the expected means for uniform random and spherical LADs. While 0.5 may be an appropriate theoretical value for k in mixed forests, it must be noted that the value additionally depends on lidar acquisition parameters such as LPM formulation. Solberg et al. (2009) showed, using first returns only, that their regression's slope coefficient (equivalent to $1/k$ in this context) was stable across Norway spruce development classes (1.83–1.98). However, when using both first and last returns the slope coefficient mean across development classes increased to 2.47 with a range from 1.83 to 2.69.

4.2. Estimating LAI with lidar-derived structural metrics and allometry (objective #3)

Our urban study adds to the larger body of work in natural forests suggesting that lidar is effective for measuring basic crown structural attributes (Fig. 9) such as height (e.g., Andersen, Reutebuch, & McGaughey, 2006; Edson & Wing, 2011) and crown base height (e.g., Popescu & Zhao, 2008; Reitberger, Schnörr, Krzystek, & Stilla, 2009). This is consistent with research suggesting laser return height distributions are less susceptible to increased scan angle than penetration metrics (Holmgren et al., 2003; Morsdorf et al., 2008). It is likely that metrics such as crown base height are best assessed with off-nadir data and in an urban forest characterized by open-grown trees. Allometric model formulation was improved by the incorporation of leaf type information (from $r^2 = 0.78$ and RMSE = 0.48 to $r^2 = 0.87$ and RMSE = 0.39). However, the model, when applied to the watershed segments improved by a smaller margin with this increased specificity ($r^2 = 0.81$ and RMSE = 0.57 to $r^2 = 0.84$ and RMSE = 0.53). This is possibly attributable to inaccuracies in the leaf-type classification of the watershed segments. Improvement was also likely limited due to aggregation of the results to the UFORE-plot level for validation purposes.

Implementation of the crown-scale allometric method produces fine-spatial scale results that are useful for calculation of urban forest ecosystem services such as building energy-use reduction and stormwater runoff mitigation. However, a key limitation of this method, and a large source of uncertainty, is that shading coefficients have been directly estimated only for a small number of species and regions. While this coefficient is not included in Eqs. (11)–(13), it is introduced implicitly when training the model against UFORE results. Of the 108 species sampled in the field, species-specific coefficients were only available for 17, and those coefficients were not likely estimated in Southern California. The remaining species were assigned coefficients corresponding to other trees of the same genus or leaf type. We expect the empirical scaling coefficients would need to be determined for other regions and forest types in order to obtain a similar degree of accuracy. Further error may have been introduced to the models generated in this study because they do not account for variation in tree condition or crown transparency. Future gains could likely be made by combining structural measurement of crown dimensions with a lidar penetration metric correlated with crown porosity.

4.3. Comparison of models and maps (objective #4)

In this study we made field measurements of LAI using crown structural measurements plus allometry and LAI_e using gap fraction inversion of hemispherical photos. We developed lidar models that roughly mimicked each method and then validated each model against its field analog. The final objective of this study was to compare the results from each method (Table 2). We did this to estimate the error bounds on urban LAI estimates. This is not a statistically-based error bound and caution must be taken in comparing LAI and LAI_e . Nevertheless, we believe that the first-order similarity of these results indicates potential for wider application of lidar remote sensing for mapping urban LAI. Notably, it was the comparison of the two ground-based methods, which resulted in the weakest relationship in terms of RMSE and bias.

The maps (Fig. 11) illustrate the broad similarities between the methods but also highlight the key difference in spatial scale of the output. In theory, the LPM map can be generated at smaller pixel sizes. However, as pixel size decreases, the number of pixels with infinite LAI_e due to numerical overflow and the percentage of ground points actually associated with neighboring pixels will increase. Richardson et al. (2009) found that with their lidar point density and LPM formulation, they could produce an LAI map at 14 m but not at 3 m, due to the lack of ground returns in many canopy-filled pixels. These issues make the prospect of mapping individual tree LAI_e using penetration metrics difficult at the present time.

The patterns of map disagreement (Fig. 11c) clearly reflect the differences in model formulation and may shed light on which model is most appropriate for a particular application. Where canopy cover is low and clumped in isolated trees (see Fig. 11c inset) the allometric method may be better suited to capture the fine scale variability in LAI. In this scenario a pixel-level inversion of an LPM would be unduly influenced by extremely high gap fraction due to small crown size and clumped foliage. On the other hand, in areas with higher overall and relatively homogeneously distributed canopy cover, pixel-level LPMs are quite sensitive to small changes in leaf surface due to the nature of the logarithmic inversion. Further, in those areas, segmentation algorithms preceding the allometric approach are less likely to properly delineate overlapping crowns so the utility of leaf type classification is diminished.

5. Conclusions

This study demonstrated the potential for mapping Leaf Area Index (LAI) in a heterogeneous urban environment using two theoretically distinct methods. We first showed strong agreement between effective

LAI (LAI_e) estimated from a laser penetration metric (LPM) and LAI_e measured in the field using hemispherical photography ($r^2 = 0.82$). In order to quantify the relationship between the two methods, we developed novel methods to correct for off-nadir pulse angles and plot-level clumping in a structurally diverse and discontinuous canopy. While we initially made use of a lidar dataset with very high point density (22 pts m^{-2}), we found that the results could be reproduced at decimated point densities down to 2 pts m^{-2} . This indicates that cities may have success implementing LPM methodology for calculating LAI_e using existing data.

Secondly, we showed that lidar-derived structural metrics such as height, crown base height, and crown segment area can be used as inputs to existing allometric equations for prediction of LAI. This result was compared against LAI allometrically estimated from field measurements of individual trees and yielded an r^2 of 0.84 when formulating separate models for each leaf type. A key difference in the mapped outputs between the methods was the spatial resolution. We found that a map produced using LPMs must have a pixel size large enough to allow for lidar beam penetration to ground, even under dense canopy. An allometric map has no theoretical lower bound on the size of the output crown object. However, maps generated using allometric equations are subject to an unknown amount of error associated with use of coefficients not developed for the trees or site in question. Thus, while this work demonstrates that LAI can be mapped at citywide scales, it is still important that the practitioner be aware of the trade-offs inherent in each of the methods. The ability to map LAI across large urban areas offers new potential to constrain estimates from hydrological and atmospheric models and better understand the spatial distribution of urban ecosystem services at increasingly fine scale.

Acknowledgements

This research was funded by the Naval Postgraduate School (N00244-11-1-0028), the National Science Foundation (BCS-0948914), and the Garden Club of America Fellowship in Urban Forestry. Special thanks to Seth Gorelik and Keri Opalk for their assistance with field data collection, David Nowak for suggestions to improve the technical methods, and the good people of Santa Barbara for allowing us on their lawns.

Appendix A. Supplementary data

Supplementary data to this article can be found online at <http://dx.doi.org/10.1016/j.rse.2015.02.025>.

References

- Alonso, M., Bookhagen, B., & Roberts, D. A. (2014). Urban tree species mapping using hyperspectral and lidar data fusion. *Remote Sensing of Environment*, 148, 70–83.
- Andersen, H. -E., Reutebuch, S. E., & McGaughey, R. J. (2006). A rigorous assessment of tree height measurements obtained using airborne lidar and conventional field methods. *Canadian Journal of Remote Sensing*, 32(5), 355–366.
- Baldocchi, D. D., Hicks, B., & Camara, P. (1987). A canopy stomatal resistance model for gaseous deposition to vegetated surfaces. *Atmospheric Environment* (1967), 21(1), 91–101.
- Bréda, N. J. J. (2003). Ground-based measurements of leaf area index: a review of methods, instruments and current controversies. *Journal of Experimental Botany*, 54(392), 2403–2417.
- Carlson, T., & Ripley, D. (1997). On the relation between NDVI, fractional vegetation cover, and leaf area index. *Remote Sensing of Environment*, 62(3), 241–252.
- Chapman, L. (2007). Potential applications of near infra-red hemispherical imagery in forest environments. *Agricultural and Forest Meteorology*, 143(1–2), 151–156.
- Chen, Q., Baldocchi, D., Gong, P., & Kelly, M. (2006). Isolating individual trees in a Savanna woodland using small footprint lidar data. *Photogrammetric Engineering & Remote Sensing*, 72(8), 923–932.
- Chen, J. M., & Black, T. (1991). Measuring leaf area index of plant canopies with branch architecture. *Agricultural and Forest Meteorology*, 57(1953), 1–12.
- Chen, J. M., & Black, T. (1992). Defining leaf area index for non-flat leaves. *Plant, Cell & Environment*, 15, 421–429.
- Chen, J. M., Rich, P. M., Gower, S. T., Norman, J. M., & Plummer, S. (1997). Leaf area index of boreal forests: Theory, techniques, and measurements. *Journal of Geophysical Research*, 102(D24), 29429.

- Edson, C., & Wing, M. G. (2011). Airborne Light Detection and Ranging (LiDAR) for Individual Tree Stem Location, Height, and Biomass Measurements. *Remote Sensing*, 3(12), 2494–2528.
- Escobedo, F. J., & Nowak, D. J. (2009). Spatial heterogeneity and air pollution removal by an urban forest. *Landscape and Urban Planning*, 90(3–4), 102–110.
- Falster, D. S., & Westoby, M. (2003). Leaf size and angle vary widely across species: what consequences for light interception? *New Phytologist*, 158(3), 509–525.
- Georgi, J. N., & Zafiriadis, K. (2006). The impact of park trees on microclimate in urban areas. *Urban Ecosystems*, 9, 195–209.
- Gower, S., Kucharik, C., & Norman, J. (1999). Direct and indirect estimation of leaf area index, fapar, and net primary production of terrestrial ecosystems. *Remote Sensing of Environment*, 42(7)(99).
- Green, R. O., Eastwood, M. L., Sarture, C., Chrien, T. G., Aronsson, M., Chippendale, B., et al. (1998). Imaging spectroscopy and the airborne visible/infrared imaging spectrometer (AVIRIS). *Remote Sensing of Environment*, 65(3), 227–248.
- Grimmond, C., Blackett, M., Best, M., Barlow, J., Baik, J., Belcher, S., et al. (2010). The international urban energy balance models comparison project: first results from phase 1. *Journal of Applied Meteorology and Climatology*, 49, 1268–1291.
- Hardin, P. J., & Jensen, R. R. (2007). The effect of urban leaf area on summertime urban surface kinetic temperatures: A Terre Haute case study. *Urban Forestry & Urban Greening*, 6(2), 63–72.
- Hirabayashi, S., Kroll, C. N., & Nowak, D. J. (2011). Component-based development and sensitivity analyses of an air pollutant dry deposition model. *Environmental Modelling & Software*, 26(6), 804–816.
- Holmgren, J., Nilsson, M., & Olsson, H. (2003). Simulating the effects of lidar scanning angle for estimation of mean tree height and canopy closure. *Canadian Journal of Remote Sensing*, 29(5), 623–632.
- Hopkinson, C., & Chasmer, L. (2009). Testing LiDAR models of fractional cover across multiple forest ecoregions. *Remote Sensing of Environment*, 113(1), 275–288.
- Hopkinson, C., Lovell, J., Chasmer, L., Jupp, D., Kljun, N., & van Gorsel, E. (2013). Integrating terrestrial and airborne lidar to calibrate a 3D canopy model of effective leaf area index. *Remote Sensing of Environment*, 136, 301–314.
- Jensen, R. R., Hardin, P. J., Bekker, M., Farnes, D. S., Lulla, V., & Hardin, A. J. (2009). Modeling urban leaf area index with AISA + hyperspectral data. *Applied Geography*, 29(3), 320–332.
- Jensen, R. R., Hardin, P. J., & Hardin, A. J. (2012). Estimating urban leaf area index (LAI) of individual trees with hyperspectral data. *Photogrammetric Engineering & Remote Sensing*, 78(5), 495–504.
- Jonckheere, I., Fleck, S., Nackaerts, K., Muys, B., Coppin, P., Weiss, M., et al. (2004). Review of methods for in situ leaf area index determination. *Agricultural and Forest Meteorology*, 121(1–2), 19–35.
- Jonckheere, I., Nackaerts, K., Muys, B., & Coppin, P. (2005). Assessment of automatic gap fraction estimation of forests from digital hemispherical photography. *Agricultural and Forest Meteorology*, 132(1–2), 96–114.
- Korhonen, L., Korpela, I., Heiskanen, J., & Maltamo, M. (2011). Airborne discrete-return LiDAR data in the estimation of vertical canopy cover, angular canopy closure and leaf area index. *Remote Sensing of Environment*, 115(4), 1065–1080.
- Lovell, J., Jupp, D., Culvenor, D. S., & Coops, N. C. (2003). Using airborne and ground-based ranging lidar to measure canopy structure in Australian forests. *Canadian Journal of Remote Sensing*, 29(5), 607–622.
- Lu, D., & Weng, Q. (2006). Spectral mixture analysis of ASTER images for examining the relationship between urban thermal features and biophysical descriptors in Indianapolis, Indiana, USA. *Remote Sensing of Environment*, 104(2), 157–167.
- Manning, W. J. (2008). Plants in urban ecosystems: Essential role of urban forests in urban metabolism and succession toward sustainability. *The International Journal of Sustainable Development and World Ecology*, 15(4), 362–370.
- McCarthy, H. R., & Pataki, D. E. (2010). Drivers of variability in water use of native and non-native urban trees in the greater Los Angeles area. *Urban Ecosystems*, 13(4), 393–414.
- Miller, J. B. (1967). *A formula for average foliage density*.
- McPherson, E. G., Simpson, J. R., Xiao, Q., & Wu, C. (2011). Million trees Los Angeles canopy cover and benefit assessment. *Landscape and Urban Planning*, 99(1), 40–50.
- Morsdorf, F., Frey, O., Meier, E., & Itten, K. (2008). Assessment of the influence of flying altitude and scan angle on biophysical vegetation products derived from airborne laser scanning. *International Journal of Remote Sensing*, 29(5), 1387–1406.
- Morsdorf, F., Kotz, B., Meier, E., Itten, K., & Allgower, B. (2006). Estimation of LAI and fractional cover from small footprint airborne laser scanning data based on gap fraction. *Remote Sensing of Environment*, 104(1), 50–61.
- Myint, S. W., Brazel, A., Okin, G., & Buyantuyev, A. (2010). Combined effects of impervious surface and vegetation cover on air temperature variations in a rapidly expanding desert city. *GIScience & Remote Sensing*, 47(3), 301–320.
- Nowak, D. J. (1996). Estimating leaf area and leaf biomass of open-grown deciduous urban trees. *Forest Science*, 42(4).
- Nowak, D. J., Crane, D. E., Stevens, J., Hoehn, R. E., Walton, J., & Bond, J. (2008a). A ground-based method of assessing urban forest structure and ecosystem services. *Arboriculture & Urban Forestry*, 34(6), 347–358.
- Nowak, D. J., Walton, J., Stevens, J., Crane, D. E., & Hoehn, R. E. (2008b). Effect of plot and sample size on timing and precision of urban forest assessments. *Arboriculture & Urban Forestry*, 34(6), 386–390.
- Oke, T. (1989). The micrometeorology of the urban forest. *Philosophical Transactions of the Royal Society of London. Series B, Biological Sciences*, 324(1223), 335–349.
- Osmond, P. (2009). Application of near-infrared hemispherical photography to estimate leaf area index of urban vegetation. *International conference on urban climate* (pp. 1–4).
- Pekin, B., & Macfarlane, C. (2009). Measurement of crown cover and leaf area index using digital cover photography and its application to remote sensing. *Remote Sensing*, 1(4), 1298–1320.
- Peper, P. J., & McPherson, E. G. (2003). Evaluation of four methods for estimating leaf area of isolated trees. *Urban Forestry & Urban Greening*, 2(1), 19–29.
- Peters, E. B., & McFadden, J. P. (2010). Influence of seasonality and vegetation type on suburban microclimates. *Urban Ecosystems*, 13(4), 443–460.
- Popescu, S. C., & Zhao, K. (2008). A voxel-based lidar method for estimating crown base height for deciduous and pine trees. *Remote Sensing of Environment*, 112(3), 767–781.
- Reitberger, J., Schnörr, C., Krzystek, P., & Stilla, U. (2009). 3D segmentation of single trees exploiting full waveform LiDAR data. *ISPRS Journal of Photogrammetry and Remote Sensing*, 64(6), 561–574.
- Richardson, J. J., Moskal, L. M., & Kim, S. -H. (2009). Modeling approaches to estimate effective leaf area index from aerial discrete-return LiDAR. *Agricultural and Forest Meteorology*, 149(6–7), 1152–1160.
- Roy, S., Byrne, J., & Pickering, C. (2012). A systematic quantitative review of urban tree benefits, costs, and assessment methods across cities in different climatic zones. *Urban Forestry & Urban Greening*, 11(4), 351–363.
- Ryu, Y., Nilson, T., Kobayashi, H., Sonnentag, O., Law, B. E., & Baldocchi, D. (2010a). On the correct estimation of effective leaf area index: Does it reveal information on clumping effects? *Agricultural and Forest Meteorology*, 150(3), 463–472.
- Ryu, Y., Sonnentag, O., Nilson, T., Vargas, R., Kobayashi, H., Wenk, R., et al. (2010b). How to quantify tree leaf area index in an open savanna ecosystem: A multi-instrument and multi-model approach. *Agricultural and Forest Meteorology*, 150(1), 63–76.
- Simpson, J. (2002). Improved estimates of tree-shade effects on residential energy use. *Energy and Buildings*, 34(10), 1067–1076. [http://dx.doi.org/10.1016/S0378-7788\(02\)00028-2](http://dx.doi.org/10.1016/S0378-7788(02)00028-2).
- Solberg, S., Brunner, A., Hanssen, K. H., Lange, H., Næsset, E., Rautiainen, M., et al. (2009). Mapping LAI in a Norway spruce forest using airborne laser scanning. *Remote Sensing of Environment*, 113(11), 2317–2327.
- Solberg, S., Næsset, E., Hanssen, K. H., & Christiansen, E. (2006). Mapping defoliation during a severe insect attack on Scots pine using airborne laser scanning. *Remote Sensing of Environment*, 102(3–4), 364–376.
- Urban, J. (1992). Bringing order to the technical dysfunction within the urban forest. *Journal of Arboriculture*, 18(2), 85–90.
- Van Gardingen, P. R., Jackson, G. E., Hernandez-Daumas, S., Russell, G., & Sharp, L. (1999). Leaf area index estimates obtained for clumped canopies using hemispherical photography. *Agricultural and Forest Meteorology*, 94(3–4), 243–257.
- Xiao, Q., & McPherson, E. G. (2002). Rainfall interception by Santa Monica's municipal urban forest. *Urban Ecosystems*, 6, 291–302.
- Zhang, Y., Chen, J. M., & Miller, J. R. (2005). Determining digital hemispherical photograph exposure for leaf area index estimation. *Agricultural and Forest Meteorology*, 133(1–4), 166–181.
- Zhao, K., & Popescu, S. C. (2009). Lidar-based mapping of leaf area index and its use for validating GLOBCARBON satellite LAI product in a temperate forest of the southern USA. *Remote Sensing of Environment*, 113(8), 1628–1645.